Phenomenology of wall-bounded Newtonian turbulence

Victor S. L'vov,* Anna Pomyalov,† and Itamar Procaccia‡
Department of Chemical Physics, The Weizmann Institute of Science, Rehovot 76100, Israel

Sergej S. Zilitinkevich§
Division of Atmospheric Sciences Department of Physical Sciences, University of Helsinki, 00101 Helsinki, Finland
(Received 27 June 2005; published 19 January 2006)

We construct a simple analytic model for wall-bounded turbulence, containing only four adjustable parameters. Two of these parameters are responsible for the viscous dissipation of the components of the Reynolds stress tensor. The other two parameters control the nonlinear relaxation of these objects. The model offers an analytic description of the profiles of the mean velocity and the correlation functions of velocity fluctuations in the entire boundary region, from the viscous sublayer, through the buffer layer, and further into the log-law turbulent region. In particular, the model predicts a very simple distribution of the turbulent kinetic energy in the log-law region between the velocity components: the streamwise component contains a half of the total energy whereas the wall-normal and cross-stream components contain a quarter each. In addition, the model predicts a very simple relation between the von Kármán slope κ and the turbulent velocity in the log-law region v^+ (in wall units): $v^+=6\kappa$. These predictions are in excellent agreement with direct numerical simulation data and with recent laboratory experiments.

DOI: 10.1103/PhysRevE.73.016303 PACS number(s): 47.27.nb, 47.27.Jv, 47.10.−g, 47.27.E−

I. INTRODUCTION

The tremendous amount of work devoted to understanding the apparent experimental *deviations* from the classical phenomenology of homogeneous and isotropic turbulence[1,2] tends to obscure the fact that in many respects this phenomenology is almost right on the mark. Starting with the basic ideas of Richardson and Kolmogorov and continuing with a large number of ingenious closures, one can offer a reasonable set of predictions regarding the statistical properties of the highly complex phenomenon of homogenous and isotropic turbulence. Thus one predicts the range of scales for which viscous effects are negligible (the so-called "inertial range" of turbulence), the crossover scale below which dissipative effects are crucial (also known as the "Kolmogorov scale"), the exact form of the third-order structure function $S_3(R)$ (third moment of the longitudinal velocity difference across a scale R), including numerical prefactors, and an approximate form of structure function of other orders $S_n(R)$ (predicted to scale like $R^{n/3}$ but showing deviations in the scaling exponents which grow with the order, giving rise to much of the theoretical work alluded to above). In particular much effort has been devoted to calculating the so-called "Kolmogorov constant" C_2 which is the prefactor of the second-order structure function, with closure approximations (see, e.g., Refs. [3,4]) coming reasonably close to its experimental estimate. Notwithstanding the deviations from the classical phenomenology, one can state that it provides a reasonable first-order estimate of many nontrivial aspects of homogeneous and isotropic turbulence. In contrast, the phenomenological theory of wall-bounded turbulence is less advanced. In reality most turbulent flows are bounded by one or more solid surfaces, making wall-bounded turbulence a problem of paramount importance. Evidently, a huge amount of literature dealt with problem, with much ingenuity and considerable success [5]. In particular one refers to von Kármán's log law of the wall which describes the profile of the mean velocity as a function of the distance from the wall. It appears, however, that the literature lacks an analytically tractable model of wall-bounded flows whose predictions can be trusted at a level comparable to the phenomenological theory of homogeneous turbulence.

In this paper we attempt to reduce this gap. We offer a phenomenological theory of wall-bounded flows that is based on standard ideas [5]; nevertheless, we develop the theory slightly further than anything that exists currently in the literature. Our central ambition is to offer a model that describes, for wall-bounded turbulent flows, the profile of mean flow and the statistics of turbulence on the level of simultaneous, one-point, second-order velocity correlation functions. In other words, the objects that we are after are the entries of the Reynolds-stress tensor *as a function of the distance from the wall*. The model will be presented for plain geometry; this geometry is relevant for a wide variety of turbulent flows, like channel and plain Couette flows, fluid flows over inclined planes under gravity (modeling river flows), atmospheric turbulent boundary layers over flat planes, and, in the limit of large Reynolds numbers, many other turbulent flows, including pipe, circular Couette flows, etc. Our model is a version of "algebraic Reynolds-stress models" [5], similar, for example, to the model proposed in [6]. The main difference is that all the previous models focused their attention on a description of the turbulent log-law

*Electronic address: Victor.Lvov@Weizmann.ac.il; URL:http://lvov.weizmann.ac.il
†Electronic address: Anna.Pomyalov@Weizmann.ac.il
‡Electronic address: ItamarProcaccia@Weizmann.ac.il; URL:http://www.weizmann.ac.il/chemphys/cfprocac/home.html
§Electronic address: Sergej.Zilitinkevich@fmi.fi

region. Separate models were then developed for the near-wall region [7], followed by interpolations of the final results to connect to the log-law region. We aim here for a consistent description that is able to properly describe the entire turbulent boundary layer from the near-wall viscous layer through the buffer layer up to the fully developed turbulent log-law region. In particular we want to capture important buffer layer characteristics like the peak in the turbulent kinetic energy which cannot result from any interpolation procedure between the viscous and log-law regions.

In developing the model we will stress analytical tractability; in other words, we will introduce approximations in order to achieve a model whose properties and predictions can be understood without resort to numerical calculations. Nevertheless, we will show that the model appears very dependable in the sense that its predictions check very well in comparison to direct numerical simulations (DNS), including some rather nontrivial predictions that are corroborated only by very recent simulations and experiments (which only now reach the sufficient accuracy and high Reynolds numbers).

In Sec. II we formulate; in Sec. II A we introduce notations and recall the equations describing the mechanical balance; in Sec. II B, we state the assumptions and detail the approximations used in the context of the balance equations for the components of the Reynolds-stress tensor W_{ij}. The result of these considerations is a set of five equations for the mean shear S and W_{ij} which is described in Sec. II C. For actual calculations this set of equations is still too rich since it contains 12 adjustable parameters. Eight of these parameters control the nonlinear behavior of the system in the outer layer and four additional parameters govern the energy dissipation in the viscous sublayer. Clearly, further reduction of the model is called for. This is accomplished in Sec. III. First, in Sec. III A we consider the full 12-parametrical solution of the model and present a comparison with experimental observations in Sec. III A 4. This comparison indicates that an adequate description of the entire turbulent boundary layer phenomenology can be achieved with only four parameters instead of 12. We refer to the four-parameter model as the "minimal model." In Sec. III B we reap the benefit of the minimal model: we find the simple and physically transparent equations (3.15) for the profiles of the Reynolds-stress tensor $W_{ij}(y)$ and the mean shear $S(y)$ (y is the distance from the wall) in terms of the root mean square of the turbulent velocity $v \equiv \sqrt{W_{ii}}$. Unfortunately, the equation for the $v(y)$profile is quite cumbersome and cannot be solved analytically. Nevertheless, we employ an effective iteration procedure that allows reaching highly accurate solutions with one or at most two iteration steps.

Section IV is devoted to a comparison of the predictions of the minimal model with results of experiments and direct numerical simulations. In particular, in Sec. IV B we show that the model describes the mean velocity profile in a channel flow with 1% accuracy almost everywhere. Only in the core does the model fail to describe the peak of the mean velocity that occurs around 5–6 wall units [independently of Reynolds number (Re)]. For our purposes this mismatch in not essential. In Sec. IV C we show that the minimal model provides a good qualitative description of the kinetic energy profile, including position, amplitude, and width of the peak of the kinetic energy in the buffer layer. In Sec. IV D we show that with the same set of four parameters the model offers also a good qualitative description of the Reynolds-stress profiles and the profiles of "partial" kinetic energies (in the streamwise, wall-normal, and cross-stream directions) almost in the entire channel. The final Sec. V presents a short summary of our results, including a discussion of the limitations of the minimal model. Possible improvements of the suggested model will have to start by addressing these limitations.

II. FORMULATION OF THE MODEL

Our starting point is the standard Reynolds decomposion [5] of the fluid velocity $\boldsymbol{U}(\boldsymbol{r},t)$ into its average (over time) $\boldsymbol{V}$ and the fluctuating components $\boldsymbol{u}$. In wall-bounded planar geometry the mean velocity is oriented in the (streamwise) $\hat{\mathbf{x}}$ direction, depending on the vertical (wall-normal) coordinate y only:

$$\boldsymbol{U}(\boldsymbol{r},t) = \boldsymbol{V}(y) + \boldsymbol{u}(\boldsymbol{r},t), \quad \boldsymbol{V}(y) \equiv \langle \boldsymbol{U}(\boldsymbol{r},t)\rangle = \hat{\mathbf{x}} V(y). \tag{2.1}$$

The mean velocity and the fluctuating parts are used to construct the objects of the theory which are the components of the Reynolds-stress tensor $\boldsymbol{W}(y)$ and the mean shear:

$$W_{ij}(y) \equiv \langle u_i u_j \rangle, \quad S(y) \equiv \frac{dV(y)}{dy}. \tag{2.2}$$

We note that in previous applications [8–16] we have employed a model in which only the trace of $\boldsymbol{W}(y)$ and its xy components were kept in a simplified description. For the present purposes we consider all the components of this tensor, paying a price of having more equations to balance, but reaping the benefit of a significantly improved phenomenology. We discuss now the equations relating these variables to each other.

A. Equation for the mechanical balance

The first equation relates the Reynolds stress W_{xy} to the mean shear; it describes the balance of the flux of mechanical momentum, and it follows as an exact result from Navier-Stokes equations and has the familiar form

$$-W_{xy}(y) + \nu_0 S(y) = P(y). \tag{2.3a}$$

W_{xy} on the left-hand side (LHS) is the turbulent (reversible) contribution to the momentum flux whereas $\nu_0 S(y)$ is the viscous (dissipative) contribution to the momentum flux. The RHS is the momentum flux generated by the pressure head. In a channel flow with the pressure gradient $p' = -dp/dx$,

$$P(y) = p'(L - y). \tag{2.3b}$$

Here L is the half width of the channel. For large Reynolds numbers near the wall one can neglect the y dependence of $P(y)$, replacing $P(y)$ by its value at the wall: $P(y) \Rightarrow P_0 \equiv P(0)$.

B. Balance of the Reynolds tensor

The next set of equations relates the various components of the Reynolds tensor $W_{ij}(y)$ defined by Eq. (2.2). In con-

trast to Eq. (2.3a) this set of equations is only partially exact. We need to model some of the terms, as explained below. We start from the Navier-Stokes equations and write the following set of equations:

$$\frac{dW_{ij}}{dt} + \epsilon_{ij} + I_{ij} = -S(W_{iy}\delta_{jx} + W_{jy}\delta_{ix}). \tag{2.4a}$$

The RHS of these equations is exact, describing the production term in the equations for $W_{ix}=W_{xi}$ which is caused by the existence of a mean shear. On the LHS of Eq. (2.4a),

$$\epsilon_{ij} = 2\nu_0 \left\langle \frac{\partial u_i}{\partial x_k}\frac{\partial u_j}{\partial x_k} \right\rangle \tag{2.4b}$$

is the exact term presenting the viscous energy dissipation. The problem is that ϵ_{ij} involve new objects, which requires evaluation via W_{ij}. This can be easily, done in regions where the velocity field is rather smooth, and in particular in the viscous sublayer, the velocity gradient exists and thus the spatial derivatives in Eq. (2.4b) are estimated using a characteristic length which is the distance from the wall y. In order to write equalities we employ the dimensionless constants $a_{ij} \simeq 1$:

$$\epsilon_{ij} \Rightarrow \epsilon_{ij}^{\mathrm{vis}} = \gamma_{ij}^{\mathrm{vis}} W_{ij}, \quad \gamma_{ij}^{\mathrm{vis}} \simeq \nu_0 \left(\frac{a_{ij}}{y}\right)^2. \tag{2.4c}$$

In general the constants a_{ij} are different for every i,j.

In the buffer sublayer and in the log-law turbulent region the energy cascades down the scales until it dissipates at the Kolmogorov (inner) scale that is much smaller than the distance y from the wall. Therefore the main contribution to the dissipation ϵ_{ij} from all scales smaller than y is due to the energy flux—i.e., has a *nonlinear character*. Due to the asymptotical isotropy of fine-scale turbulence, the nonlinear contribution should be diagonal in i, j (see, e.g., [5]):

$$\epsilon_{ij} \Rightarrow \epsilon_{ij}^{\mathrm{nl}} = \gamma \frac{W}{3}\delta_{ij}, \quad W \equiv \mathrm{Tr}\{\boldsymbol{W}\}, \tag{2.5a}$$

where the prefactor $\frac{1}{3}$ is introduced to simplify equations below. The characteristic "nonlinear flux frequency" γ can be estimated using a standard Kolmogorov 41-dimensional analysis:

$$\gamma(y) = \frac{b}{y}\sqrt{W(y)}, \tag{2.5b}$$

again with some constants $b \sim 1$. The "outer scale" of turbulence is estimated in Eq. (2.5b) by the only available characteristic length y, the distance to the wall.

As one sees from Eq. (2.5), the dissipation of particular component of the Reynolds-stress tensor—say, W_{xx}—depends not only on W_{xx} itself, but also on other components, W_{yy} and W_{zz} in our case. It means that ϵ_{ij}, given by Eq. (2.5a) leads, in the framework of Eq. (2.4), not only to the dissipation of total energy, but also to its redistribution between different components of W_{ii}. In order to separate these effects we divide ϵ_{ij} into two parts as follows:

$$\epsilon_{ij}^{\mathrm{nl}} = \epsilon_{ij}^{\mathrm{nl},1} + \epsilon_{ij}^{\mathrm{nl},2}, \tag{2.6a}$$

$$\epsilon_{ij}^{\mathrm{nl},1} = \gamma W_{ij}\delta_{ij}, \tag{2.6b}$$

$$\epsilon_{ij}^{\mathrm{nl},2} = -\gamma\left(W_{ij} - \delta_{ij}\frac{W}{3}\right)\delta_{ij}. \tag{2.6c}$$

Clearly, $\epsilon_{ij}^{\mathrm{nl},1}$ describes the damping of each component W_{ii} separately, without changing of their ratios, while the traceless part $\epsilon_{ij}^{\mathrm{nl},2}$ does not contribute to the dissipation of total energy and leads only to a redistribution of energy between components of the Reynolds-stress tensor. This contribution we will include into the "return to isotropy" term (2.13b), that will be discussed below.

Actually, we presented ϵ_{ij} as the sum

$$\epsilon_{ij} = \epsilon_{ij}^{\mathrm{dis}} + \epsilon_{ij}^{\mathrm{nl},2}, \tag{2.7}$$

in which for the total energy dissipation is responsible only first term on the RHS. In the buffer layer both contributions to $\epsilon_{ij}^{\mathrm{dis}}$—the viscous dissipation $\epsilon_{ij}^{\mathrm{vis}}$ and the nonlinear one $\epsilon_{ij}^{\mathrm{nl},1}$—are important. Their relative role depending on the teurbulent statistics. We will employ two simple interpolation formulas which lead to two versions of the minimal model:

$$\epsilon_{ij}^{\mathrm{dis}} = \Gamma_{ij} W_{ij}, \tag{2.8}$$

$$\Gamma_{ij}(y) = \gamma_{ij}^{\mathrm{vis}}(y) + \gamma(y)\delta_{ij}, \quad \text{"sum,"} \tag{2.9}$$

$$\Gamma_{ij}(y) = \sqrt{\gamma_{ij,\mathrm{vis}}^2(y) + \gamma^2(y)\delta_{ij}}, \quad \text{"root."} \tag{2.10}$$

The versions of the resulting model will be referred to as the "sum" and "root" versions correspondingly. *A priori* there is no reason to prefer one or the other, and we leave the choice for later, after the comparisons with the data.

The term I_{ij} in Eq. (2.4a) is caused by the pressure-strain correlations

$$I_{ij} = -\frac{1}{\rho_0}\left\langle p\left(\frac{\partial u_i}{\partial x_j} + \frac{\partial u_j}{\partial x_i}\right)\right\rangle, \tag{2.11}$$

and is known in the literature as the "return to isotropy" [5]. Due to incompressibly the constraint I_{ij} is a traceless tensor and therefore does not contribute to the total energy balance, leading only to a redistribution of the partial kinetic energy between different vectorial components. Also, this term does not exist in isotropic turbulence where $W_{ij}=1/3\,W\delta_{ij}$. We adopt the simplest linear Rota approximation for the "return to isotropy" term [5], using once more different characteristic frequencies $\bar{\gamma}_{ij}$, estimated as follows:

$$I_{ij} = \bar{\gamma}_{ij}(3W_{ij} - \delta_{ij}W), \tag{2.12a}$$

$$\bar{\gamma}_{ij}(y) \equiv \bar{b}_{ij}\frac{\sqrt{W(y)}}{y}, \quad \bar{b}_{ij} \simeq 1. \tag{2.12b}$$

One sees that I_{ij} has precisely the same structure as $\epsilon_{ij}^{\mathrm{nl},2}$, introduced by Eq. (2.6c). Therefore it is convenient to treat these contributions together, introducing

$$\tilde{I}_{ij} \equiv I_{ij} + \epsilon_{ij}^{\mathrm{nl},2}, \tag{2.13a}$$

$$\tilde{I}_{ij} \equiv \tilde{\gamma}_{ij}(3W_{ij} - \delta_{ij}W), \tag{2.13b}$$

$$\tilde{\gamma}_{ij}(y) \equiv \tilde{b}_{ij}\frac{\sqrt{W(y)}}{y}, \quad \tilde{b}_{ij} = \bar{b}_{ij} - \frac{b}{3}\delta_{ij}. \tag{2.13c}$$

Recall that the tensor $\tilde{I}_{ij}$ must have zero trace for any values of W_{ij}. This is possible only if $\tilde{b}_{xx}=\tilde{b}_{yy}=\tilde{b}_{zz}\equiv\tilde{b}_{\rm d}$, $\tilde{b}_{xy}\equiv\tilde{b}$, and consequently

$$\tilde{\gamma}_{xx} = \tilde{\gamma}_{yy} = \tilde{\gamma}_{zz} \equiv \tilde{\gamma}_{\rm d}, \quad \tilde{\gamma}_{xy} \equiv \tilde{\gamma}. \tag{2.14}$$

Thus, representation (2.13b) involves only two free parameters $\tilde{b}_{\rm d}$ and $\tilde{b}$.

Equations (2.4) for W_{ij} with $ij=xx,yy,zz$, and xy involve seven constants a_{ij}, b, $\tilde{b}_{\rm d}$, and $\tilde{b}$. Our goal is to formulate the simplest possible model, with a minimal number of adjustable constants. The strategy will be now to use experimental and simulational data, coupled with reasonable physical considerations, to reduce the number of parameters to 4, each being responsible for a separate fragment of the underlying physics.

We should stress that we neglect in Eq. (2.4a) the spatial energy transport term $\epsilon_{\rm tr}$, caused by the tripple-velocity correlations, pressure-velocity correlations, and the viscosity [5]. In the high-Re_λ limit the density of turbulent kinetic energy becomes space independent in the log-law region. Accordingly, the spatial transport term is very small in that log-law region. A more detailed analysis (see, e.g., Fig. 3 in Ref. [17]) shows that even for a relatively small Re_λ in the log-law turbulent region this term is small with respect to the energy transfer term from scale to scale which is represented by γW_{ij} in the equations above. On the other hand, in the viscous sublayer the mean velocity is determined by the viscous term and thus the influence of the spatial energy transfer term can be again neglected. To keep the model simple we will neglect $\epsilon_{\rm tr}$ term also in the buffer layer where it is of the same order as the other terms of the model. The reason for this simplification, which evidently will cause some trouble in the buffer layer, is that the energy balance equations used below become local in space. This is a great advantage of the model, allowing us to advance analytically to obtain a very transparent phenomenology of wall-bounded turbulence. It was already demonstrated in Ref. [14] that the simple description (2.9) gives a uniformly reasonable description of the rate of the energy dissipation in the entire boundary layer. Here we improve this description further, effectively accounting for the energy transfer term in the balance equation by an appropriate decrease in the viscous layer parameters a_{ij}.

C. Summary of the two versions of the model

For the sake of further analysis we present the model with the final notation:

$$-W_{xy}(y) + \nu_0 S(y) = P(y), \tag{2.15a}$$

$$[\Gamma_{xx} + 3\tilde{\gamma}_{\rm d}]W_{xx} = \tilde{\gamma}_{\rm d}W - 2SW_{xy}, \tag{2.15b}$$

$$[\Gamma_{yy} + 3\tilde{\gamma}_{\rm d}]W_{yy} = \tilde{\gamma}_{\rm d}W, \tag{2.15c}$$

$$[\Gamma_{zz} + 3\tilde{\gamma}_{\rm d}]W_{zz} = \tilde{\gamma}_{\rm d}W, \tag{2.15d}$$

$$[\Gamma_{xy} + 3\tilde{\gamma}]W_{xy} = -SW_{yy}. \tag{2.15e}$$

In the traditional theory of wall-bounded turbulence one employs the "wall units" u_τ, τ and ℓ_τ for the velocity, time, and length [5] which for a fluid of density ρ are

$$u_\tau \equiv \sqrt{\frac{P_0}{\rho}}, \quad \tau \equiv \frac{\nu_0}{P_0}, \quad \ell_\tau \equiv \frac{\nu_0}{\sqrt{\rho P_0}}. \tag{2.16}$$

Using these scales one defines the wall-normalized dimensionless objects

$$y^+ \equiv \frac{y}{\ell_\tau}, \quad V^+(y) \equiv \frac{V_x(y)}{u_\tau}, \quad v_{\rm T}^+(y) \equiv \frac{v_{\rm T}(y)}{u_\tau}, \quad \text{etc.},$$

$$S^+ \equiv S\tau, \quad W_{ij}^+(y) \equiv \frac{W_{ij}(y)}{u_\tau^2}, \quad \text{etc.} \tag{2.17}$$

In our model we can use the property of locality in space to introduce "local units":

$$\tilde{u}_\tau(y) \equiv \sqrt{\frac{P(y)}{\rho}}, \quad \tilde{\tau}(y) \equiv \frac{\nu_0}{P(y)}, \quad \tilde{\ell}_\tau(y) \equiv \frac{\nu_0}{\sqrt{\rho P(y)}}, \tag{2.18}$$

similar to traditional wall units, Eq. (2.16), but with the replacement $P_0 \to P(y)$, and "locally normalized" dimensionless objects, analogous to Eq. (2.17):

$$y^\ddagger \equiv \frac{y}{\tilde{\ell}_\tau(y)}, \quad v_{\rm T}^\ddagger(y^\ddagger) \equiv \frac{v_{\rm T}(y)}{\tilde{u}_\tau(y)},$$

$$S^\ddagger(y^\ddagger) \equiv S\tilde{\tau}(y), \quad W_{ij}^\ddagger(y^\ddagger) \equiv \frac{W_{ij}(y)}{\tilde{u}_\tau^2(y)}, \quad \text{etc.} \tag{2.19}$$

Then the dimensionless version of Eq. (2.15a) reduces to

$$-W_{xy}^\ddagger + S^\ddagger = 1, \tag{2.20a}$$

$$(\Gamma_{xx}^\ddagger + 3\tilde{\gamma}_{\rm d}^\ddagger)W_{xx}^\ddagger = \tilde{\gamma}_{\rm d}^\ddagger W^\ddagger - 2S^\ddagger W_{xy}^\ddagger, \tag{2.20b}$$

$$(\Gamma_{yy}^\ddagger + 3\tilde{\gamma}_{\rm d})W_{yy}^\ddagger = \tilde{\gamma}_{\rm d}W^\ddagger, \tag{2.20c}$$

$$(\Gamma_{zz}^\ddagger + 3\tilde{\gamma}_{\rm d}^\ddagger)W_{zz} = \tilde{\gamma}_{\rm d}^\ddagger W^\ddagger, \tag{2.20d}$$

$$(\Gamma_{xy}^\ddagger + 3\tilde{\gamma}^\ddagger)W_{xy}^\ddagger = -S^\ddagger W_{yy}^\ddagger. \tag{2.20e}$$

Introducing $v^\ddagger \equiv \sqrt{W^\ddagger}$ we can write

$$\Gamma_{ij}^\ddagger = \left(\frac{a_{ij}}{y^\ddagger}\right)^2 + \frac{bv^\ddagger}{y^\ddagger}\delta_{ij}, \quad \text{for the sum model,} \tag{2.21a}$$

$$\Gamma_{ij}^\ddagger = \sqrt{\frac{a_{ij}^4}{(y^\ddagger)^4} + \frac{b^2 v^{\ddagger 2}}{(y^\ddagger)^2}\delta_{ij}}, \quad \text{for the root model,} \tag{2.21b}$$

$$\tilde{\gamma}_{\rm d}^\ddagger = \frac{\tilde{b}_{\rm d}v^\ddagger}{y^\ddagger}, \quad \tilde{\gamma}^\ddagger = \frac{\tilde{b}v^\ddagger}{y^\ddagger}, \quad \text{for both versions.} \tag{2.21c}$$

III. ANALYSIS OF THE MODEL

A. Solution of the seven-parameters version of the model

1. Solutions in the viscous sublayer

The four equations (2.15b), (2.15c), (2.15d), and (2.15e) can be considered as a homogeneous "linear" set of equations for W_{xx}, W_{yy}, W_{zz}, and W_{xy} (with coefficients that are functions of W). They can have a trivial solution $W=0$ for which Eq. (2.15a) gives

$$S = P_0/\nu_0, \quad V = yP_0/\nu_0, \quad W_{ij} = 0, \Rightarrow \text{ laminal layer}. \tag{3.1}$$

The complete absence of turbulent activity in the viscous layer in our model is a consequence of leaving out the energy transport in physical space.

2. Analysis of the turbulent solution

Equations (2.20b), (2.20c), (2.20d), and (2.20e) have a nontrivial "turbulent solution" with $W^\ddagger \neq 0$:

$$W^\ddagger_{xx} = \frac{W^\ddagger}{2}\left[\frac{\Gamma^\ddagger_{yy}+\tilde{\gamma}^\ddagger_{\rm d}}{\Gamma^\ddagger_{yy}+3\tilde{\gamma}^\ddagger_{\rm d}} + \frac{\Gamma^\ddagger_{zz}+\tilde{\gamma}^\ddagger_{\rm d}}{\Gamma^\ddagger_{zz}+3\tilde{\gamma}^\ddagger_{\rm d}}\right], \tag{3.2a}$$

$$W^\ddagger_{yy} = \frac{W^\ddagger\tilde{\gamma}^\ddagger_{\rm d}}{\Gamma^\ddagger_{yy}+3\tilde{\gamma}^\ddagger_{\rm d}}, \quad W^\ddagger_{zz} = \frac{W^\ddagger\tilde{\gamma}^\ddagger_{\rm d}}{\Gamma^\ddagger_{zz}+3\tilde{\gamma}^\ddagger_{\rm d}}, \tag{3.2b}$$

$$W^\ddagger_{xy} = \frac{-W^\ddagger S^\ddagger\tilde{\gamma}^\ddagger_{\rm d}}{(\Gamma^\ddagger_{xy}+3\tilde{\gamma}^\ddagger)(\Gamma^\ddagger_{yy}+3\tilde{\gamma}^\ddagger_{\rm d})}, \tag{3.2c}$$

if its determinant Δ vanishes. The solvability condition $\Delta=0$ gives

$$(S^\ddagger)^2 = \frac{\Gamma^\ddagger_{xy}+3\tilde{\gamma}^\ddagger_{xy}}{2\tilde{\gamma}^\ddagger_{yy}(\Gamma^\ddagger_{zz}+3\tilde{\gamma}^\ddagger_{zz})}[\Gamma^\ddagger_{xx}\Gamma^\ddagger_{yy}\Gamma^\ddagger_{zz} + 2\tilde{\gamma}^\ddagger_{\rm d}(\Gamma^\ddagger_{xx}\Gamma^\ddagger_{yy}+\Gamma^\ddagger_{xx}\Gamma^\ddagger_{zz} + \Gamma^\ddagger_{yy}\Gamma^\ddagger_{zz}) + 3(\tilde{\gamma}^\ddagger_{\rm d})^2(\Gamma^\ddagger_{xx}+\Gamma^\ddagger_{yy}+\Gamma^\ddagger_{zz})]. \tag{3.2d}$$

Substitution $W^\ddagger_{xy}$ and $S^\ddagger$ in Eq. (2.20a) gives a closed equation for the function $W^\ddagger(y^\ddagger)$ (or for $v^\ddagger \equiv \sqrt{W^\ddagger}$). To present the resulting equation in explicit form, introduce

$$A(v^\ddagger) \equiv S^\ddagger/v^\ddagger, \quad B(v^\ddagger) \equiv -W^\ddagger_{xy}/S^\ddagger v^\ddagger,$$

$$R_{ij} \equiv \Gamma^\ddagger_{ij}/v^\ddagger, \quad \tilde{r}_{\rm d} \equiv \tilde{\gamma}^\ddagger_{\rm d}/v^\ddagger, \quad \tilde{r} \equiv \tilde{\gamma}^\ddagger/v^\ddagger. \tag{3.3}$$

Using Eqs. (3.2d) and (3.2c) we find

$$A^2(v^\ddagger) = \frac{R_{xy}+3\tilde{r}}{2\tilde{r}_{\rm d}(R_{zz}+3\tilde{r}_{\rm d})}[R_{xx}R_{yy}R_{zz} + 2\tilde{r}_{\rm d}(R_{xx}R_{yy}+R_{xx}R_{zz} + R_{yy}R_{zz}) + 3\tilde{r}^2_{\rm d}(R_{xx}+R_{yy}+R_{zz})],$$

$$B(v^\ddagger) = \frac{\tilde{r}_{\rm d}}{(R_{xy}+3\tilde{r})(R_{yy}+3\tilde{r}_{\rm d})}. \tag{3.4}$$

Now Eq. (2.20a) can be presented as

$$A(v^\ddagger)v^\ddagger[1+B(v^\ddagger)v^\ddagger] = 1. \tag{3.5}$$

Together with Eqs. (3.2) this provides the full solution of Eqs. (2.20).

3. Outer layer, $y^\ddagger > 50$

In the outer layer, far away from the wall, all the viscous terms in Eqs. (2.20) can be neglected. In this case Eqs. (2.21) for both the sum and root minimal models give

$$\Gamma^\ddagger_{ij} \Rightarrow \tilde{\gamma}^\ddagger\delta_{ij}, \tag{3.6}$$

and Eqs. (3.2b), (3.2c), and (3.2d) and the solution (3.15) simplify drastically:

$$W^\ddagger_{yy} = W^\ddagger_{zz} = \frac{W^\ddagger\tilde{b}_{\rm d}}{b+3\tilde{b}_{\rm d}}. \tag{3.7}$$

By analyzing the results of experiments and numerical simulations (as discussed in Sec. IV) we found that in the outer layer $W^\ddagger_{xx}=\frac{1}{2}W^\ddagger$ and $W^\ddagger_{yy}=W_{zz}=\frac{1}{4}W^\ddagger$. The model reproduces these findings if we choose

$$b = \tilde{b}_{\rm d}. \tag{3.8}$$

Using this relation and the solution of Eq. (2.20a), $W^\ddagger_{xy}=-1$, in the rest of Eqs. (2.20), one finds

$$W^\ddagger = \sqrt{\frac{24\tilde{b}}{b}}, \quad \frac{1}{\kappa} = \left(\frac{b}{2}\right)^{1/4}(3\tilde{b})^{3/4}. \tag{3.9}$$

Here κ is nothing but the von Kármán constant, which determines the slope of the logarithmic mean velocity profile in the log-law turbulent region:

$$V^+(y^+) = \kappa^{-1}\ln y^+ + C, \quad \text{for } z^+ \gtrsim 30,$$

$$\kappa \approx 0.436, \quad C \approx 6.13. \tag{3.10}$$

The experimental value of κ and the intercept C were taken from [20]. Using the simulations result $W^+ \approx 6.85$ of Ref. [17], which is reproduced in Fig. 6, we find

$$b \approx 0.256, \quad \tilde{b} \approx 0.500. \tag{3.11}$$

4. Reduction of the number parameters: The minimal model

The parameters a_{ij} are responsible for the difference between the energy dissipation and the energy transfer in the viscous sublayer. To further simplify the model we reduce the number of independent parameters a_{ij} from 4 (a_{xx}, a_{yy}, a_{zz}, and a_{xy}) to 2, denoted as a and $\tilde{a}$. Among various possibilities [including $a_{xx}=a_{zz}=a$, $a_{yy}=\tilde{a}$, $a_{xy}=(a+\tilde{a})/2$] we choose a parametrization similar to the situation with the outer layer parameters:

$$a_{ii} = a, \quad a_{xy} = \tilde{a}. \tag{3.12}$$

The analytical solution given in next section III B simplifies considerably with the four-parameter version of the model. A further simplification $a=\tilde{a}$ could be considered, but we rule it out since it yields a monotonic dependence of the turbulent kinetic energy $W^+(y^+)$ with y^+, while experimentally there is a pronounced peak of $W^+(y^+)$ in the buffer sublayer; see Sec. IV C. We thus consider the four-parameter model as the "minimal model" (MM).

Below we will use mostly the following set of constants:

$$a = 1.0, \quad \widetilde{a} = 10.67, \quad \text{sum MM}, \tag{3.13a}$$

$$a = 1.0, \quad \widetilde{a} = 12.95, \quad \text{root MM}, \tag{3.13b}$$

$$b = 0.256, \quad \widetilde{b} = 0.500, \quad \text{both MMs}. \tag{3.13c}$$

This choice is based on the analysis of the simulational and experimental data presented in Sec. IV.

Notice that eliminating b from Eqs. (3.9) (valid for both sum and root models) one gets

$$v^{\ddagger} = 12\kappa\widetilde{b} \approx 6\kappa. \tag{3.14}$$

With the simulational values $\kappa=0.436$ and $W^{\ddagger}_{\infty}=6.85$ this relationship is valid with a precision that is better than 1%.

B. Analysis of the minimal models

1. $a,\widetilde{a}$ parametrization of the general solution

With the minimal parametrization, given by Eq. (3.12), the solution (3.2) takes on a simpler form:

$$W^{\ddagger}_{yy} = W^{\ddagger}_{zz} = \frac{v^{\ddagger}}{4v_4}W^{\ddagger}, \quad W^{\ddagger}_{xx} = \frac{v_2}{2v_4}W^{\ddagger}, \tag{3.15a}$$

$$W^{\ddagger}_{xy} = -\frac{W^{\ddagger}}{2}\sqrt{\frac{bv^{\ddagger}v_1}{\widetilde{6b}v_3v_4}}, \quad S^{\ddagger} = \frac{1}{y^{\ddagger}}\sqrt{\frac{6b\widetilde{b}v_1v_3v_4}{v^{\ddagger}}}. \tag{3.15b}$$

Here we introduced the following shorthand notation v_j for the sum MM:

$$v_1 \equiv v^{\ddagger} + \frac{a^2}{by^{\ddagger}}, \quad v_2 \equiv v^{\ddagger} + \frac{a^2}{2by^{\ddagger}},$$

$$v_3 \equiv v^{\ddagger} + \frac{\widetilde{a}^2}{3\widetilde{b}y^{\ddagger}}, \quad v_4 \equiv v^{\ddagger} + \frac{a^2}{4by^{\ddagger}}. \tag{3.16a}$$

For the root MM instead of Eq. (3.16a) we take

$$v_1 \equiv \sqrt{v^{\ddagger 2} + \frac{a^4}{(by^{\ddagger})^2}}, \quad v_2 \equiv \frac{v_1 + v^{\ddagger}}{2}, \quad v_4 \equiv \frac{v_1 + 3v^{\ddagger}}{4},$$

$$v_3 \equiv \frac{v^{\ddagger}b}{\widetilde{b}} + \sqrt{(\widetilde{b}-b)^2v^{\ddagger 2} + \frac{\widetilde{a}^4}{(3\widetilde{b}y^{\ddagger})^2}}. \tag{3.16b}$$

With the minimal parametrization Eq. (3.5) takes a very simple explicit form

$$v^{\ddagger 2} + \frac{12\widetilde{b}v^{\ddagger}}{y^{\ddagger}}r_3r_4 = \sqrt{\frac{24\widetilde{b}r_3r_4}{br_1}}, \quad r_j \equiv v_j/v^{\ddagger}. \tag{3.17a}$$

This form of the equation for $v^{\dagger}_{\mathrm{T}}$ serves below as a starting point for an approximate (iterative) analytical solution. One can also seek an exact solution by numerical methods; to this aim, it is better to use the following form of the same equation:

$$F(v^{\ddagger}, y^{\ddagger}) \equiv \frac{b}{24\widetilde{b}}v^{\ddagger 6}v_1 + v^{\ddagger}v_3v_4\left[\frac{b}{y}v^{\ddagger 2}v_1 - 1\right] + \frac{6b\widetilde{b}}{y^2}v_1v_3^2v_4^2 = 0. \tag{3.17b}$$

Equation (3.17b) has seven roots for the sum MM, (and 27 for the root MM) but only two of them, denoted as $v^{\ddagger}_{\pm}$, are real and positive for large enough $y^{\ddagger}$. These two roots approach each other upon decreasing the distance from the wall. At some value of $y^{\ddagger}$ these roots merge:

$$v^{\ddagger}_{+}(y_{\mathrm{vs}}) = v^{\ddagger}_{-}(y_{\mathrm{vs}}) \equiv v_* < v^{\ddagger}_{\infty}. \tag{3.18}$$

The values y_{vs} and v_* as functions of the problem parameters follow from the polynomial (3.17b):

$$F(v^{\ddagger}, y^{\ddagger}) = 0, \quad \frac{\partial F(v^{\ddagger}, y^{\ddagger})}{\partial v^{\ddagger}} = 0. \tag{3.19}$$

For $y^{\ddagger} < y_{\mathrm{vs}}$ there are no physical (positive-definite) solutions of Eq. (3.17b). This is a laminar region that was discussed before as the viscous sublayer. In Table II, below, we present the corresponding values of y_{vs} and v_* for $b=0.256, \widetilde{b}=0.5$ and various pairs of a, $\widetilde{a}$.

2. Iterative solution of Eq. (3.17a) for rms turbulent velocity $v^{\ddagger}(y^{\ddagger})$

To develop further analytic insight we employ an iterative procedure to find an approximate solution for $v^{\ddagger}_{+}(y)$ for all $y^{\ddagger} > y_{\mathrm{vs}}$, outside a narrow region (of width less than unity) about y_{vs}. For this goal we forget for a moment that r_j depends on $v^{\ddagger}$ and consider Eq. (3.17a) as a quadratic equation with a positive solution:

$$v^{\ddagger} = \sqrt{\sqrt{\frac{24\widetilde{b}r_3r_4}{br_1}} + \left(\frac{6\widetilde{b}r_3r_4}{y^{\ddagger}}\right)^2} - \frac{6\widetilde{b}r_3r_4}{y^{\ddagger}}. \tag{3.20}$$

However, r_j does depend on $v^{\ddagger}$. For example, for the sum MM,

$$r_1(v^{\ddagger}) = 1 + \frac{a^2}{by^{\ddagger}v^{\ddagger}_{\mathrm{T}}}, \quad r_2(v^{\ddagger}) = 1 + \frac{a^2}{2by^{\ddagger}v^{\ddagger}},$$

$$r_3(v^{\ddagger}) \equiv 1 + \frac{\widetilde{a}^2}{3\widetilde{b}y^{\ddagger}v^{\ddagger}}, \quad r_4(v^{\ddagger}) = 1 + \frac{a^2}{4by^{\ddagger}v^{\ddagger}}. \tag{3.21}$$

Nevertheless, for very large $y^{\ddagger}$ all $r_j \to 1$ and an asymptotic solution of Eq. (3.20) reproduces the asymptotic value of $v^{\ddagger}=v^{\ddagger}_{\infty}=(24\widetilde{b}/b)^{1/4}$, given by Eq. (3.9).

A much better approximation for $v^{\ddagger}(y^{\ddagger})$ (denoted as $v^{\ddagger}_1$) is obtained using in Ref. (3.20) a $v^{\ddagger}$-independent $r_{j,0} \equiv r_j(v^{\ddagger}_{\infty})$ instead of $r_j=1$:

$$v^{\ddagger}_1 = \sqrt{\sqrt{\frac{24\widetilde{b}r_{3,0}r_{4,0}}{br_{1,0}}} + \left(\frac{6\widetilde{b}r_{3,0}r_{4,0}}{y^{\ddagger}}\right)^2} - \frac{6\widetilde{b}r_{3,0}r_{4,0}}{y^{\ddagger}}. \tag{3.22a}$$

Clearly, this iterative procedure can be prolonged further and one can find the velocity $v^{\ddagger}$ at the $n+1$ iteration step,

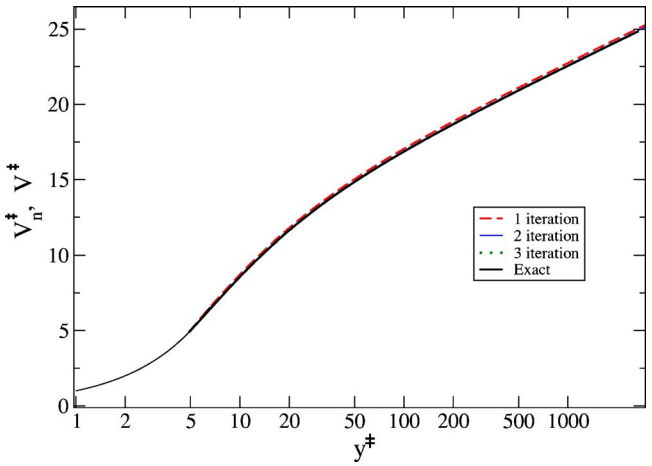

FIG. 1. (Color online) Log plots of the exact solution for mean velocity profile $V^{\ddagger}(y^{\ddagger})$ and approximate profiles $V_n^{\ddagger}(y^{\ddagger})$, computed on the nth iteration step for $n=1,2,3,4$ for the sum MM with constants, taken from Eq. (3.11). All plots practically coincides within the linewidth.

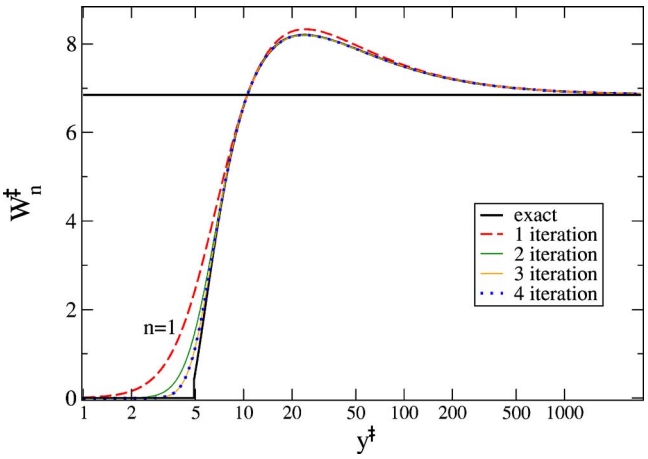

FIG. 2. (Color online) Log-plots of the iterative $W_n^{\ddagger}$, $n=1$–4 and "exact" numerical solutions (thick solid line) for the trace of the Reynolds tensor in the sum MM with constants, taken from Eq. (3.11). Plots for $W_3^{\ddagger}$ and $W_4^{\ddagger}$ coincide within the linewidth.

$v_{n+1}^{\ddagger}(y^{\ddagger})$, using the relations $r_{j,n} \equiv r_j(v_n^{\ddagger})$, found with the velocity $v_n^{\ddagger}$ of the previous, nth step:

$$v_{n+1}^{\ddagger} = \sqrt{\sqrt{\frac{24\tilde{b}r_{3,n}r_{4,n}}{br_{1,n}} + \left(\frac{6\tilde{b}r_{3,n}r_{4,n}}{y^{\ddagger}}\right)^2} - \frac{6\tilde{b}r_{3,n}r_{4,n}}{y^{\ddagger}}}. \tag{3.22b}$$

The numerical verification of the iteration procedure is given in the Appendix . The conclusion is that already the first few iterations are sufficiently accurate for all practical purposes: often one can use the first iteration and occasionally the second one.

Remarkably, the first iteration can be formulated directly in terms of the basic Eqs. (2.20) by replacing the turbulent velocity profile $v^{\ddagger}(y^{\ddagger})$ in Eqs. (2.21) for $\Gamma_{ij}^{\ddagger}$ and $\tilde{\gamma}_{ij}^{\ddagger}$ by its asymptotic value in log-law region $v_{\infty}^{\ddagger}=(24\tilde{b}/b)^{1/4}$.

3. Iterative solution for the mean velocity and Reynolds tensor profiles

Consider first the resulting plots for the mean velocity profile, $V_n^{\ddagger}(y^{\ddagger})$, computed with the help of turbulent velocity $v_n^{\ddagger}$ at the nth iteration step:

$$V_n^{\ddagger}(y^{\ddagger}) = y_{\mathrm{vs}} + \int_{y_{\mathrm{vs}}}^{y^{\ddagger}} S_n^{\ddagger}(\xi)d\xi, \quad y^{\ddagger} > y_{\mathrm{vs}}. \tag{3.23}$$

Here $S_n^{\ddagger}(x)$ denotes $S^{\ddagger}(x)$, given by Eqs. (3.15), with $v^{\ddagger}=v_n^{\ddagger}$. Figure 1 displays plots of $V_n^{\ddagger}(y^{\ddagger})$ for $n=1,2,3,4$ and the "exact" (numerical) result $V^{\ddagger}(y^{\ddagger})$. All the plots almost coincide within the linewidth. This means that for the purpose of computing $V^{\ddagger}(y^{\ddagger})$ one can use the first approximation $v_1^{\ddagger}$ given by Eq. (3.22a) instead of the exact solution $v^{\ddagger}$.

Next we present in Fig. 2 log plots for the trace of the Reynolds-stress tensor $W_n^{\ddagger}(y^{\ddagger})$, (computed with the nth iteration step for $n=1,2,3,4$) together with the "exact" numerical solution $W^{\ddagger}(y^{\ddagger})$ for the sum MM. Evidently, the iterative procedure for the kinetic energy does not converge as rapidly as for the mean velocity profile: one can distinguish the plots of $W_1^{\ddagger}(y^{\ddagger})$, $W_2^{\ddagger}(y^{\ddagger})$, and $W_3^{\ddagger}(y^{\ddagger})$; the plots of $W_3^{\ddagger}(y^{\ddagger})$ and $W_4^{\ddagger}(y^{\ddagger})$ coincide within the linewidth. Nevertheless, for $y^{\ddagger}>5$ (i.e., in the buffer layer and in the outer region) already the first iterative solution provides a very reasonable approximation to the exact solution for the kinetic energy profile.

IV. ANALYSIS OF THE NUMERICAL AND EXPERIMENTAL DATA AND COMPARISON WITH THE MODEL PREDICTION

In this section we analyze and compare the predictions of the minimal models to results of experiments and comprehensive direct numerical simulations of high-Re channel flows. We refer to results that were made available in the public domain by Moser, Kim, and Mansour [17], to large-eddy-simulations performed by Casciola [18] and to recent laboratory experiments in a vertical water tunnel by Angrawal, Djenidi, and Antonia [19]. The choice of the outer layer parameters b_{ij} and $\tilde{b}_{ij}$ is based on our analysis of the anisotropy in the log-low region, presented in Sec. IV A. The relation between the viscous layer parameters a vs $\tilde{a}$ is based on the comparison between the direct numerical simulation (DNS) and model mean velocity profiles, presented in Sec. IV B. The final choice of a and $\tilde{a}$ is motivated by the DNS data for the kinetic profile which is compared with the model prediction in Sec. IV C. Section IV D is devoted to a comparison of the model results with the DNS profiles of the Reynolds stress $W_{xy}^{\ddagger}$ and partial kinetic energies $W_{xx}^{\ddagger}$, $W_{yy}^{\ddagger}$, and $W_{zz}^{\ddagger}$.

A. Anisotropy of the log-law region: Relative partial kinetic energies R_{xx}, R_{yy}, and R_{zz} in the outer layer

The anisotropy of turbulent boundary layer can be characterized by the dimensionless ratios

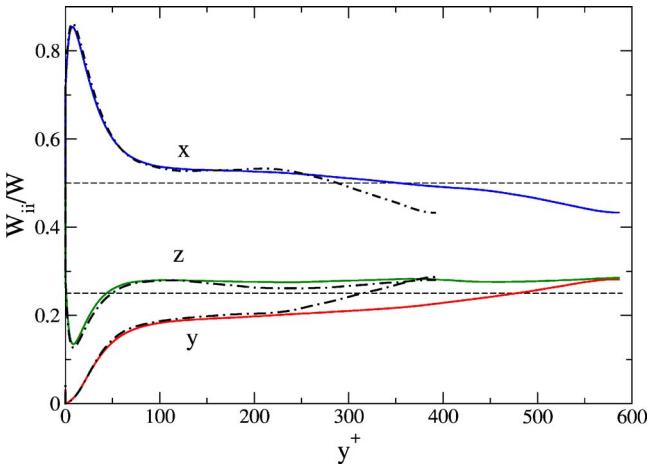

FIG. 3. (Color online) DNS profiles of the relative kinetic energies in the stream wise, wall-normal, and span wise directions R_{xx}, R_{yy}, and R_{zz}, respectively. Solid lines: $\mathrm{Re}_\lambda=590$. Dot-dashed lines: $\mathrm{Re}_\lambda=395$. Horizontal dashed lines show levels 0.5 and 0.25.

$$R_{ii}(y^+) \equiv \frac{W_{ii}(y^+)}{W(y^+)} = \frac{W^+_{ii}(y^+)}{W^+(y^+)}. \tag{4.1}$$

This anisotropy plays an important role in various phenomena and was a subject of experimental and theoretical concern for many decades; see, e.g., [1,5]. Nevertheless, up to now the dispersion of results on the subject appears quite large. There is a widely spread opinion, based on old experiments, that the wall-normal turbulent fluctuations W_{yy} are much smaller than the other ones. For example, in the classical textbook by Monin and Yaglom [1] it was reported that for a neutrally stratified log-boundary layer $R_{xx}=54\%$, $R_{yy}=6\%$, and $R_{zz}=40\%$. This definitely contradicts recent DNS results for $\mathrm{Re}_\lambda=590$ which are available in Ref. [17], as shown in Fig. 3. Note that there is a region about $100<y^+<\frac{2}{3}\mathrm{Re}_\lambda$ where the plots of $R_{ii}(y^+)$ are nearly horizontal, as expected in the log-law region. From these plots we can conclude that is this region $R_{xx}\approx 53\%$ which is close to the value 54%, stated in [1]. Nevertheless, the DNS data for R_{yy} and $\mathcal{R}_{zz}$ are completely different. From Fig. 3 one gets $\mathcal{R}_{yy}\approx 22\%$ and $\mathcal{R}_{zz}\approx 27\%$. Thus $\mathcal{R}_{yy}$ can be considered roughly equal to $\mathcal{R}_{zz}$. We should mention here that various models of turbulent boundary layers give $\mathcal{R}_{yy}=\mathcal{R}_{zz}$ in the asymptotic log-law region. We propose that the difference between $\mathcal{R}_{yy}$ and $\mathcal{R}_{zz}$ which is observed in Fig. 3 is due to the effect of the energy transfer. This effect practically vanishes in the asymptotic limit $\mathrm{Re}_\lambda\to\infty$, but is still present at values of Re_λ which are available in DNS [17]. Indeed, for both values of Re_λ shown in Fig. 3, $W_{yy}=W_{zz}$ in the center of the channel, where the energy flux vanishes by symmetry. Clearly, there is no energy flux also in space homogeneous cases; for example, for a constant shear flow, in which, according to the model, one should expect $W_{yy}=W_{zz}$ in the entire space.

Our expectation that $W_{yy}=W_{zz}$, which is based on symmetry considerations, is confirmed by the large-eddy simulation (LES) of the constant shear flow [18]. As one sees in Fig. 4 in this flow $\mathcal{R}_{xx}\approx 0.46$, while $W_{yy}\approx W_{zz}\approx 0.27$.

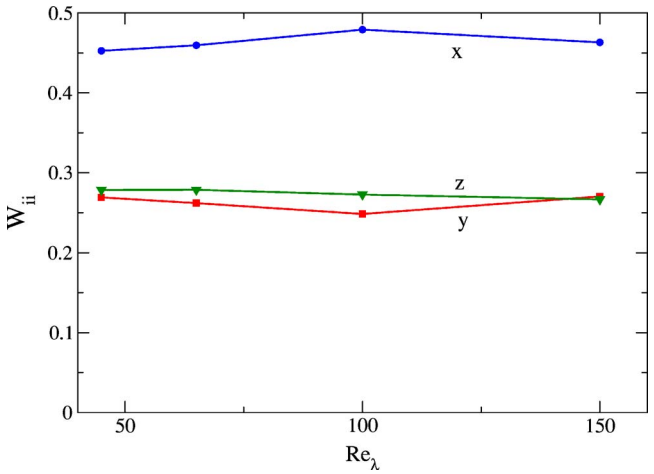

FIG. 4. (Color online) Relative components of the Reynolds stress tensor $\widetilde{W}_{ii}$, Eq. (4.1), for for constant-shear flow. Results of the LES [18]. Lines serve only to guide the eye.

As stated, for sufficiently large values of Re_λ the energy transfer terms should almost vanish in the log-law region and, according to our model, one can expect in that region $W_{yy}=W_{zz}$ also in the channel flow. This viewpoint was confirmed in the aforementioned laboratory experiment [19] in a vertical water channel with $\mathrm{Re}_\lambda=1000$, reproduced in Fig. 5. The experimental values of $\mathcal{R}_{xx}$, $\mathcal{R}_{yy}$, and $\mathcal{R}_{zz}$ in the log-law turbulent region are in excellent quantitative agreement with the values $\mathcal{R}_{xx}=0.5$ and $\mathcal{R}_{yy}=\mathcal{R}_{zz}=0.25$ shown in Figs. 3 and 5 by horizontal dashed lines.

Table I summaries the DNS, LES, and experimental values of the relative kinetic energies in comparison with the model expectations. The conclusion is that, in contradiction with the old and still widespread viewpoint [1] that the wall-normal turbulent activity is strongly suppressed, $\mathcal{R}_{yy}<0.1$, the turbulent kinetic energy in the log-law region is distributed in a very simple manner: the streamwise component contains a half of total energy, $\mathcal{R}_{xx}=\frac{1}{2}$, and the rest is equally distributed between the wall-normal and spanwise compo-

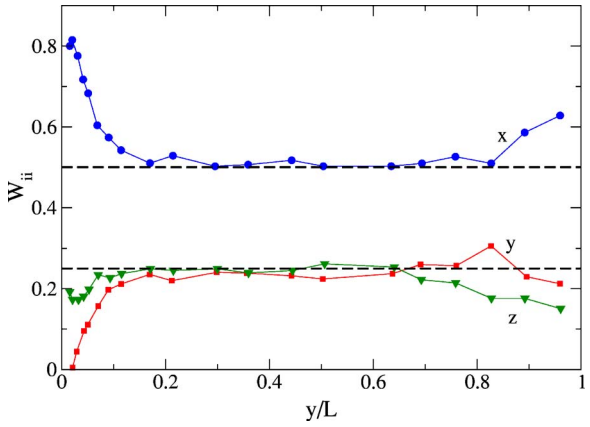

FIG. 5. (Color online) Experimental profiles of the relative kinetic energies $\mathcal{R}_{ii}$ in a vertical water channel with $\mathrm{Re}_\lambda=1000$ according to Ref. [19]. The solid lines serve to guide the eye. The dashed lines show the model prediction in the log-law region $\mathcal{R}_{xx}=0.5$ and $\mathcal{R}_{yy}=\mathcal{R}_{zz}=0.25$.

TABLE I. Asymptotic values of the relative kinetic energies $\mathcal{R}_{ii}$ in the log-law region $y^{\ddagger}>200$ taken from DNS ($\mathrm{Re}_\lambda=395,590$) [17], LES [18], and experiment in a water channel with $\mathrm{Re}_\lambda=1000$ [19]. The last column presents the predictions of the minimal model.

$R_{ii,\infty}, \downarrow ii \downarrow$	DNS (17)	LES (18)	Water channel (19)	Model
xx	≈ 0.53	≈ 0.46	0.50 ± 0.01	0.50
yy	≈ 0.22	≈ 0.27	0.25 ± 0.02	0.25
zz	≈ 0.27	≈ 0.27	0.25 ± 0.02	0.25

nents: $\mathcal{R}_{yy}=\mathcal{R}_{zz}=\frac{1}{2}$. As shown in Sec. III A 4, this very simple energy distribution is predicted by the minimal model if one assumes that the characteristic nonlinear times scales in the energy transfer term and in the return-to-isotropy term are identical.

B. Mean velocity profile in channel flows

To compute the mean velocity profile $V^+(y^+)$ in our approach we need to connect first $S^+(y^+)$ with $S^{\ddagger}(y^{\ddagger})$. According to the definitions (2.17)–(2.19)

$$S^+(y^+)=\left(1-\frac{y^+}{\mathrm{Re}_\lambda}\right)S^{\ddagger}\left(y^+\sqrt{1-\frac{y^+}{\mathrm{Re}_\lambda}}\right), \tag{4.2}$$

where

$$\mathrm{Re}_\lambda \equiv L/\ell_\tau \tag{4.3}$$

and $y^+>y_{\mathrm{vs}}$. For $y^+<\hat{\mathbf{y}}_{\mathrm{vs}}$ we can take $S^+(y^+)=1$ and integrate the resulting shear over the distance to the wall with the no-slip boundary condition. The resulting profiles $V^+(y^+)$ for $\mathrm{Re}_\lambda=590$ and the parameters (3.11) are shown in Fig. 6 as a dashed line for the sum MM and as a dot-dashed line for the root MM. The DNS profile of [17] for the same Re_λ is shown as a solid line. There is no significant difference (relatively less than 1%) between these plots in the viscous sublayer, buffer, and outer layers, where $y^+\lesssim 300$—i.e., in about 50% of the channel half-width $L^+=\mathrm{Re}_\lambda=590$. This robustness of the mean velocity profile $V^+(y^+)$ is a consequence of the fact that $V^+(y^+)$ is an integral of the mean shear S^+ which is described very well both in the viscous and the outer layers.

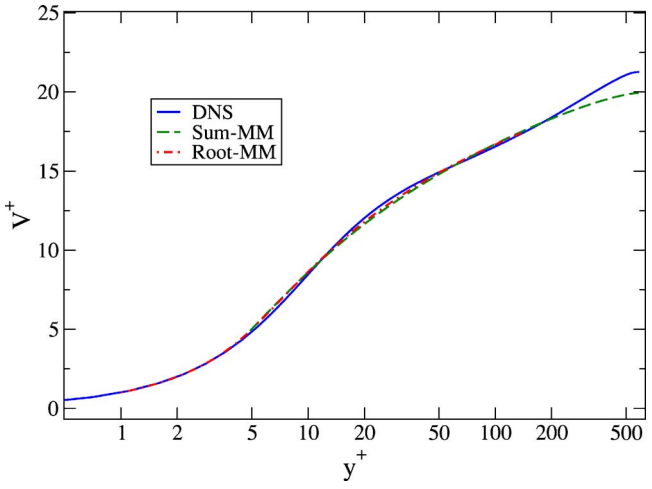

FIG. 6. (Color online) Mean velocity profiles $V^+(y^+)$: The solid blue line: DNS data [17] for $\mathrm{Re}_\tau=590$. The dashed green line: analytical profile $V^+(y^+)$ for the sum MM. Dash-dotted red line for the root MM using the parameters, Eq. (3.11). The relative deviation of the analytical predictions from the DNS data is about 1%, smaller for the root MM than for the sum MM.

Notice that our model does not describe the upward deviation from the log low which is observed near the midchannel (of about 5–6 units in V^+, independent of the Reynolds number). We consider this minor disagreement as an acceptable price for the simplicity of the minimal model which neglects the energy transport term toward the centerline of the channel. This transport is the only reason for some turbulent activity near the centerline where both the Reynolds stress W_{xy} and the mean shear S vanish due to symmetry. Just at the centerline the source term in our energy equation, $-2SW_{xy}$, is zero and the missing energy transport term is felt.

The plots in Fig. 6 have a reasonably straight logarithmic region from $y^+\approx 20$ to $y^+\approx 200$. On the other hand, the Reynolds-stress profile at the same $\mathrm{Re}_\lambda=590$ shown in Fig. 8, below, has no flat region at all. Such a flat region is expected in the true asymptotic regime of $\mathrm{Re}_\lambda\to\infty$, where $W^+=-1$. Therefore, if one plots the model profiles V^+ at different Re_λ and fits them by log-linear profiles (3.10), one can get a Re_λ dependence of the "effective" intercept in the von Kármán log law. We think that this explains why the measured value of the log-low intercept can depend on the Reynolds number and on the flow geometry (channel versus pipe): both in DNS and in physical experiments one usually does not reach high enough values of Re_λ.

C. Profiles of the total kinetic energy density and the choice of the pair $a,\tilde{a}$

The quality of the profiles $V^+(y^+)$ calls for a bit more thinking. In fact, one find that the minimal model produces practically the same profiles $V^+(y^+)$ not only for the parameters (3.13) but for a wide choice of the pairs $a,\tilde{a}$—for example, for $a=2$ and $\tilde{a}=8.6$. Actually, for any $0\leqslant a\leqslant 4$ one can find a value of $\tilde{a}$ that gives a mean velocity profile in good agreement with Fig. 6. In other words, in the $(a,\tilde{a})$ plane there exists a long narrow corridor that produces a good quantitative description of $V^+(y^+)$. Within this corridor there exists a line that provides a "best fit" of $V^+(y^+)$, minimizing the mean-square deviation δV^+,

$$\delta V^+ \equiv \sqrt{\langle [V^+_{\mathrm{MM}}(y^+)-V^+_{\mathrm{DNS}}(y^+)]^2\rangle}, \tag{4.4}$$

of the model prediction $V^+_{\mathrm{MM}}(y^+)$ from the DNS profile $V^+_{\mathrm{DNS}}(y^+)$ in the inner region $y^+<50$. Some of the best pairs are given in Table II together with the corresponding values of δV^+. Table II also presents values of y_{vs} and v_*; recall that for $y^{\ddagger}<y_{\mathrm{vs}}, v^{\ddagger}=0$, for $y^{\ddagger}=y_{\mathrm{vs}}+0$ there is a jump of $v^{\ddagger}$ from zero to $v^{\ddagger}=v_*$. The most striking difference for different $(a,\tilde{a})$ pairs is in the behavior of the Reynolds stress profiles $W^{\ddagger}(y^{\ddagger})$ that can be used to select the best values of these parameters.

TABLE II. Optimal values of $\tilde{a}$ for a given value of a, that δV^+ of Eq. (4.4). For optimal pairs $(a,\tilde{a})$ in the sum and the root versions of the minimal model (denoted as Σ and $\sqrt{}$ correspondingly) we present the values y_{vs} of $y^\ddagger$, separating the viscous solution with $v^\ddagger=0$ from turbulent regime with $v_* \equiv v^\ddagger(y_{vs}+0)$. The last two columns present the $y^\ddagger$ position, y_{max}, of the maximum of the kinetic energy and the corresponding values of $W^\ddagger_{max} \equiv W^\ddagger(y_{max})$.

MM	a	$\tilde{a}$	$\delta V^\ddagger$	y_{vs}	v_*	y_{max}	$W^\ddagger_{max}$
Σ	0.1	10.4	0.29	1.5	0.017	21	8.33
$\sqrt{}$	0.1	12.0	0.25	1.1	0.008	18	8.32
Σ	0.25	10.9	0.25	2.4	0.061	22	8.48
$\sqrt{}$	0.25	12.1	0.25	2.1	0.016	19	8.36
Σ	0.5	11.1	0.25	3.4	0.159	22	8.47
$\sqrt{}$	0.5	12.6	0.17	3.4	0.247	19	8.50
Σ	1.0	10.7	0.22	4.8	0.401	24.6	8.24
$\sqrt{}$	1.0	12.9	0.15	4.9	0.234	19.2	8.59
Σ	1.5	9.7	0.20	5.7	0.600	27	7.76
$\sqrt{}$	1.5	12.9	0.16	4.8	0.743	19	8.58
Σ	2.0	8.6	0.19	6.4	0.783	27	7.26
$\sqrt{}$	2.0	11.8	0.17	6.7	0.743	20	8.13
Σ	4.0	2.9	0.21	7.2	0.630	–	–
$\sqrt{}$	4.0	6.3	0.46	8.5	1.04	–	–

Clearly, the minimal model with only four fit parameters cannot fit perfectly the profiles of all the physical quantities that can be measured. Therefore the actual values of a and $\tilde{a}$ should be determined with a choice of the characteristics of turbulent boundary layers that we desire to describe best. Foremost in any modeling should be the mean velocity profile which is of crucial importance in a wide variety of transport phenomena. Next we opt to fit well the profile of the kinetic energy density [or, equivalently, the profile of the Reynolds stress tensor trace $W^\ddagger(y^\ddagger)$]. Figure 7, upper panel, shows the DNS profiles of the trace of the Reynold-stress tensor $W^+(y^+)$ for $\mathrm{Re}_\lambda=590$ (solid lower line) and $\mathrm{Re}_\lambda=395$ (dashed lower line). There are no plateaus in these plots, meaning that these values of Re_λ are not large enough to have a true scale-invariant log-law region. Nevertheless, the plots of

$$W^\ddagger(y^+) = \left(1 - \frac{y^+}{\mathrm{Re}_\lambda}\right)^{-1} W^+(y^+) \tag{4.5}$$

(shown in the same upper panel of Fig. 7) display clear plateaus, according to the theoretical prediction for $\mathrm{Re}_\lambda \to \infty$.

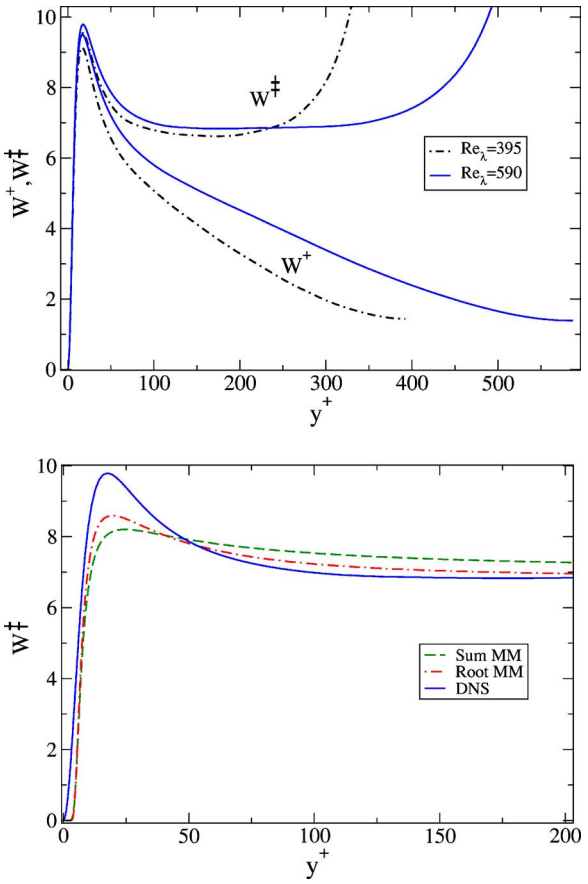

FIG. 7. (Color online) Upper panel: DNS profiles of the trace of the Reynolds-stress tensor (twice of the total kinetic energy densities) in two normalizations, W^+ and $W^\ddagger$. Solid blue line: $\mathrm{Re}_\tau=590$. Dot-dashed black line: $\mathrm{Re}_\tau=395$. Lower panel: comparison of the DNS profile $W^\ddagger(y^+)$ for $\mathrm{Re}_\lambda=590$ (blue solid line) with the results of the sum MM (green dashed line) and the root MM (red dot-dashed line) with constants, Eq. (3.13).

This means that the decay of $W^+(y^+)$ is related to the decrease of the momentum flux $P(y)$ and that the dimensionless "‡" variables, Eqs. (2.19), that use the y-dependent value of the momentum flux $P(y)$ represent the asymptotic physics of the wall-bounded turbulent flow, at lower values of Re_λ than the traditional "wall units" (2.17), which are based on the wall value of the momentum flux P_0.

To compare the model prediction with simulational results we have to relate $W^\ddagger_{ij}(y^\ddagger)$ with $W^+_{ij}(y^+)$ in channel flows. According to Eqs. (2.17)–(2.19)

$$W^+_{ij}(y^+) = \left(1 - \frac{y^+}{\mathrm{Re}_\lambda}\right) W^\ddagger_{ij}\left(y^+\sqrt{1 - \frac{y^+}{\mathrm{Re}_\lambda}}\right), \tag{4.6}$$

and similar equations for the its trace $W^+(y^+)$. Figure 7 shows a peak of $W^\ddagger(y^+)$, $W^\ddagger_{max} \equiv W^\ddagger(y_{max}) \approx 9.8$ at $y^+=y_{max} \approx 18$. As one sees from the Table II, the minimal model reproduces the peak in $W^\ddagger(y^\ddagger)$ with an amplitude of about 8–8.6 for $a \lesssim 2$. To be specific we choose $a=1$ in both versions of the minimal model: sum MM and root MM. With this choice we plot in Fig. 7, lower panel, both theoretical profiles $W^\ddagger_\Sigma(y^+)$ and

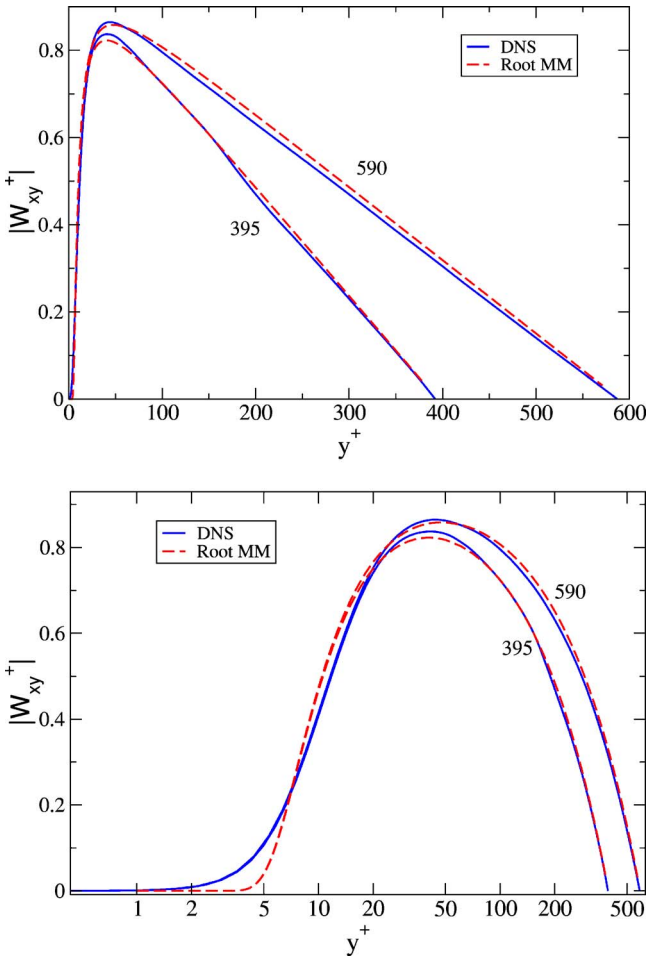

FIG. 8. (Color online) Comparison of the DNS Reynolds stress profiles $|W_{xy}^+|$ (blue solid lines) for the channel flow with $\mathrm{Re}_\lambda=395$ and 590 with the root MM profiles with constants (3.13), red dashed lines. Upper panel: linear coordinates. Lower panel: the same plots in the linear-log coordinates.

$W_{xy}^{\pm}(y^+)$ in comparison with the simulational profile $W_{xy,\mathrm{DNS}}^{\pm}(y^+)$. It appears that the root MM is in better correspondance with the simulation than the sum MM. However, for the sake of analytic calculations, the sum MM is simpler. Therefore, again, the choice of the versionof MM depends on what is more important for a particular application: calculational simplicity or accuracy of fit.

D. Profiles of the Reynolds stress tensor

In Fig. 8 we present (by solid lines) simulational profiles of the Reynolds stress $W_{xy}^+(y^+)$ for $\mathrm{Re}_\lambda=395$ and $\mathrm{Re}_\lambda=590$ in comparison with the model predictions (dashed lines) for the root MM. The upper panel shows the comparison in linear coordinates, the lower panel in linear-log coordinates, stressing the buffer layer region. In the model profiles we used the values of parameters (3.13), chosen to fit the simulational profiles for the mean velocity and the kinetic energy. In other words, in comparing the profiles of $W_{xy}^+(y^+)$ in Fig. 8 *no further fitting was exercised*. Having this in mind, we consider the agreement as very encouraging. The only difference between the model predictions and the simulational profiles of $W_{xy}^+(y^+)$ is in a steeper front of the model profiles for $y^+<20$. This is again because the model does not account for the energy transfer that can only flatten the front. As already mentioned, even for $\mathrm{Re}=590$ the maximum value of the Reynolds stress does not reach asymptotic value $|W_{xy}^+|=1$, as it should in the true log-law region. The corresponding comparison for the sum-MM looks very similar and is therefore not shown.

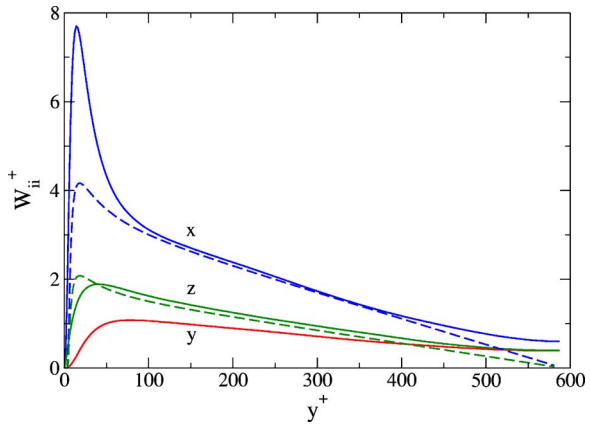

FIG. 9. (Color online) Comparison of the DNS (solid lines) and root MM results (dashed lines) for partial kinetic energies profiles in the channel flow with $\mathrm{Re}_\lambda=590$. The model parameters are taken from Eq. (3.13).

Next, we present in Fig. 9 the simulational and root MM profiles of the diagonal components of the Reynolds-stress tensor $W_{ii}^+(y^+)$ for the channel flow with $\mathrm{Re}_\lambda=590$. Solid lines present simulational profiles, dashed lines the model profiles. The streamwise and spanwise profiles $W_{xx}^+(y^+)$ and $W_{zz}^+(y^+)$ are in good agreement in the most of the channel, $70<y^+<470$, while for the wall-normal component, the model profile $W_{yy}^+(y^+)=W_{zz}^+(y^+)$ and differs from the simulational one. The model also predicts quantitatively an increase in the streamwise part of the kinetic energy and a decrease in the span wise and wall-normal components in the buffer layer which is observed in simulations. The physical reason of this is simple: as is well known, the energy from the mean flow is transferred only to the stream wise component of the turbulent fluctuations. Accordingly, in the model one sees the energy production term $(-2SW_{xy})$ only in the RHS of equation for W_{xx}. The energy redistributes between other components due to the "return-to-isotropy" term I_{ij}, Eq. (2.13b), with isotropization frequency $\propto 1/y$. The relative importance of I_{ij} (in comparison with the energy relaxation term) decreases toward the wall due to the viscous contribution $\propto 1/y^2$. Accordingly, near the wall only a small part of the kinetic energy can be transferred from the streamwise to the wall-normal and the span wise components of the velocity during the relaxation time $(\propto 1/\Gamma)$. Also, the model describes well the part (about 50% in the outer layer) of the total kinetic energy that contains the streamwise components.

In the core of the flow $(y^+>450)$ the model gives smaller values of all components W_{ii}^+, as compared to simulations and experiments. This is again because the model neglects the energy transfer toward the centerline of the channel, where

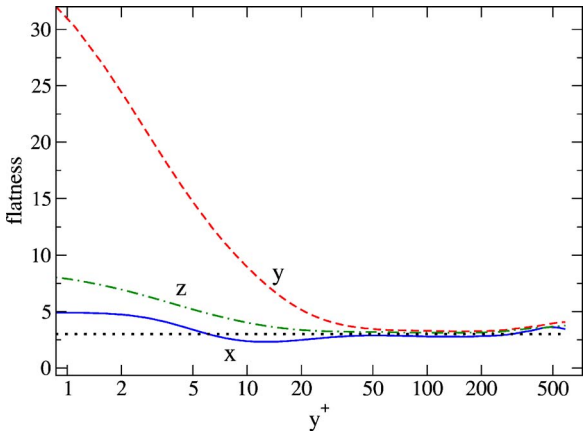

FIG. 10. (Color online) Profiles of the flatness of the x, y, and z components of the turbulent velocity fluctuations, DNS data [17] for $\mathrm{Re}_\tau=590$. The horizontal dotted line shows Gaussian value for the flatness, equal to 3.

the energy input into turbulence, $-2SW_{xy}$, disappears due to the symmetry reason.

As before, there is a quantitative disagreement between the model and simulations in the buffer layer. One can relate this with the fact that the model neglects the energy flux toward the wall, which plays a considerable role in the energy balance. The minimal models are local in space, but this effect can be effectively accounted for by an appropriate choice of the dissipation constants, taking $a_{yy}>a_{xx}=a_{zz}$. We do not propose to take this route; in the buffer layer, the turbulent flow is strongly affected by highly intermittent events (coherent structures) connected with the near-wall instabilities of the laminal sub layer. This is confirmed by the very large values of the flatness (above 30), as shown in Fig. 10. Only for $y^+>50$ does the flatness reach the Gaussian value of 3 and one can successfully utilize various lower-order closure models for describing wall-bounded flows.

V. SUMMARY: STRENGTH AND LIMITATIONS OF THE MINIMAL MODEL

The minimal model as formulated in this paper is a version of the algebraic Reynolds-stress models. Its aim is to *describe*, for wall-bounded turbulent flows, the profile of mean flow and the statistics of turbulence on the level of simultaneous, one-point, second-order velocity correlation functions—i.e., the entries of the Reynolds-stress tensor W_{ij}. The model was developed explicitly for plain geometry, including a wide variety of turbulent flows, like channel and plane Couette flows, fluid flows over inclined planes under gravity (modeling river flows), atmospheric turbulent boundary layers over flat planes, and, in the limit of large Reynolds numbers, many other turbulent flows, including pipe, circular Couette flows, etc.

In developing a simple model one needs to decide what are the physically important aspects of the flow statistics, those which determine the mean-flow and turbulent transport phenomena. The choice of the Reynolds-stress approach was dictated by the decision to emphasize an accurate description of the $V(y)$ and $W_{ij}(y)$ profiles. The main criteria in constructing the model were simplicity, physical transparency, and maximal analytical tractability of the resulting model. That is why we took liberty to ignore the spatial energy flux, and, thanks to the plain geometry, to estimate the spatial derivatives and the outer scale of turbulence using the distance to the wall y. The same motivations led to choosing the simplest linear Rotta approximation of the "return to isotropy term" [21] and the simplest dimensional form of the nonlinear term for energy flux down the scales, also in agreement with [21].

By proper parametrization the number of fit parameters was reduced from 12 to 4. Two of these, a, and $\tilde{a}$, are responsible for the viscous dissipation of the diagonal, W_{ii}, and the off-diagonal, W_{xy}, components of the Reynolds-stress tensor. The other two parameters—b and $\tilde{b}$—control the nonlinear relaxation of W_{ii} and W_{xy}. It appears that one cannot decrease the number of fit parameters further with impunity. The outer-layer parameters $b=0.256$ and $\tilde{b}=0.500$ where chosen to describe the observed constant values of von Kármán in the log law (3.10) and the asymptotic level of the density of kinetic energy. The viscous layer parameters were chosen to describe the observed values of the intersection C in the von Kármán log law (3.10) and the peak of the kinetic energy in the buffer sublayer. The resulting set of five equations for the mean shear $S(y)$, Reynolds stress W_{xy} and W_{xx}, W_{yy}, and W_{zz} with just four fit parameters is referred to as the minimal mode.

As demonstrated in Sec. IV the minimal model with the given set (3.13) of four parameters describes five functions.

(i) The mean velocity profile $V(y)$ is described with an accuracy of $\simeq 1\%$, almost throughout the channel (except of small velocity defect in the core of the flow); cf. Fig. 6.

(ii) The Reynolds stress profile $W_{xy}(y)$ is also described with an accuracy of a few percent (except in the viscous layer $y^+<5$ in which W_{xy} does not contribute to the mechanical balance); cf. Fig. 8.

(iii) The total kinetic energy profile $1/2\,W(y)$ is reproduced with reasonable (semiquantitative) accuracy, including the position and width of its peak in the buffer sublayer; cf. Fig. 7.

(iv) The profiles of the partial kinetic energies, $\frac{1}{2}W_{xx}(y)$, $\frac{1}{2}W_{yy}(y)$, and $\frac{1}{2}W_{zz}(y)$, are reproduced (see Fig. 9), including the simple $\frac{1}{2}-\frac{1}{4}-\frac{1}{4}$ distribution in the asymptotic outer region. This distribution is supported by recent experimental, DNS, and LES data, as shown in Figs. 3, 4, and 5.

We consider all this as good support of the minimal model; too much data are being reproduced to be an accident. It appears that the minimal model takes into account the essential physics almost throughout the channel flow.

On the other hand, one should accept that such a simple model cannot pretend to describe all the aspects of the turbulent statistics in wall-bounded flows. For example, the minimal model ignores the quasi-two-dimensional character of turbulence and the existence of coherent structures in the very vicinity of the wall. The minimal model does not attempt to take into account many-point and high-order turbulent statistics, including three-point velocity correlation functions and pressure-velocity correlations, responsible for the

spatial energy flux and for the isotropization of turbulence. Finally, our choice of dissipation term definitely contradicts to the near-wall expansion (and see Sec. 11.7.4 of [5]), in disagreement with various known improvements of [21]. We propose that all this is a reasonable price for the simplicity and transparency of the minimal model, which is constructed with emphasis on the fundamental characteristics $V(y)$ and $W_{ij}(y)$ which are crucial for most applications.

We trust that a proper generalization of the minimal model will be found useful in the futures in studies of more complicated turbulent flows, laden with heavy particles, bubbles, etc.

ACKNOWLEDGMENTS

We thank T.S. Lo for his critical reading of the manuscript and many insightful remarks. We are grateful to Carlo Casciola for sharing with us his LES data. We express our appreciation to R.G. Moser, J. Kim, and N.N. Mansour for making their comprehensive DNS data of high-Re channel flow available to all in Ref. [17]. This work was supported in part by the U.S. Israel Binational Scientific Foundation and the European Commission under a TMR research grant.

APPENDIX: VALIDATION OF THE ITERATIVE PROCEDURE

To see how the iterative procedure described in Sec. III B 2 works, we plotted in Fig. 11 iterative profiles of the turbulent velocity $v_n^\ddagger(y^\ddagger)$ for $n=1,\ldots,5$ together with the (numerical) solutions of Eq. (3.17a), $v_+^\ddagger(y^\ddagger)$ (the thick solid line) and $v_-^\ddagger(y^\ddagger)$ (dot-dashed curve). The horizontal straight line presents the asymptotic value $v_\infty^\ddagger$. The critical point $\{v_*^\ddagger, y_{vs}^\ddagger\}$ is shown by a black circle. Our analysis shows (and see also Fig. 11) that already the simple equation

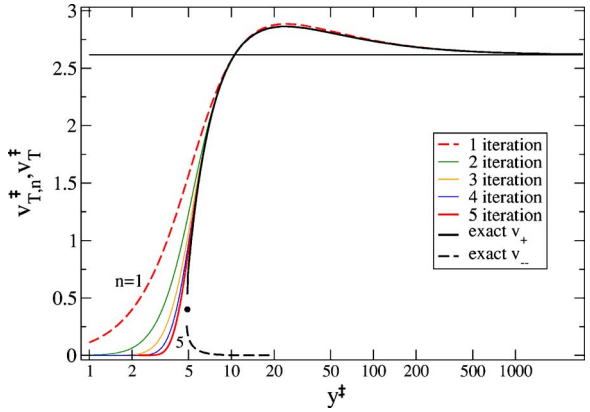

FIG. 11. (Color online) Log plots of functions $v_\infty^\ddagger \approx 2.62$ (horizontal straight line) and profiles $v_n^\ddagger(y^\ddagger)$ in the sum MM for $n=1$ (the dashed line), 2,3,4,5 together with the "exact" (numerical) solutions of Eq. (3.17a), $v_+^\ddagger(y^\ddagger)$ (the thick solid line) and $v_-^\ddagger(y^\ddagger)$ (dot-dashed line). Constants are given by Eqs. (3.13). For this choice the critical point (designated as a black circle) corresponds to $v_*^\ddagger \approx 0.4$ at $y_{vs}^\ddagger \approx 4.9$.

(3.22a) gives the relative accuracy (with respect to $v_\infty^\ddagger$) better than 1% for $y^\ddagger > 30$. The second iteration works with this accuracy in a wider region $y^\ddagger > 10$; the third iteration gives a 1% accuracy for $y^\ddagger \approx 5$, which is about the critical value $y_{vs}^\ddagger \approx 4.8$. Unexpectedly, the approximate solutions work even below the $y_{vs}^\ddagger$, where exact solution is $v^\ddagger = 0$. One observes with increasing n the widening of the region, in which $v_n^\ddagger$ is practically indistinguishable from zero. The overall conclusion from these observations is that already the fist few iterations give a very good accuracy for all practical purposes, and very often one can use only the first or the second iteration.

[1] A. S. Monin and A. M. Yaglom, *Statistical Fluid Mechanics* (MIT Press, Cambridge, MA, 1979), Vol. 1, Chap. 3.
[2] U. Frisch, *Turbulence: The Legasy of A.N. Kolmogorov* (Cambridge University Press, Cambridge, England, 1995).
[3] R. H. Kraichnan, Phys. Fluids **9**, 1728 (1966).
[4] V. Yakhot and S. A. Orszag, Phys. Rev. Lett. **57**, 1722 (1986).
[5] S. B. Pope, *Turbulent Flows* (Cambridge University Press, Cambridge, England, 2000).
[6] B. E. Launder, G. J. Reece, and W. Rodi, J. Fluid Mech. **68**, 535 (1975).
[7] B. E. Launders and W. C. Reynolds, Phys. Fluids **26**, 1157 (1983).
[8] V. S. L'vov, A. Pomyalov, I. Procaccia, and V. Tiberkevich, Phys. Rev. Lett. **92**, 244503 (2004).
[9] E. De Angelis, C. M. Casciola, V. S. L'vov, A. Pomyalov, I. Procaccia, and V. Tiberkevich, Phys. Rev. E **70**, 055301(R) (2004).
[10] R. Benzi, V. S. L'vov, I. Procaccia, and V. Tiberkevich, Europhys. Lett. **68**, 825 (2004).
[11] V. S. L'vov, A. Pomyalov, I. Procaccia, and V. Tiberkevich, Phys. Rev. E **71**, 016305 (2005).
[12] V. S. L'vov, A. Pomyalov, I. Procaccia, and V. Tiberkevich Phys. Rev. Lett. **94**, 174502 (2005).
[13] R. Benzi, E. de Angelis, V. S. L'vov, I. Procaccia, and V. Tiberkevich, J. Fluid Mech. (to be published), e-print nlin.CD/0405033.
[14] V. S. L'vov, A. Pomyalov, and V. Tiberkevich, Environ. Fluid Mech. **5**, 973 (2005).
[15] R. Benzi, E. S. C. Ching, T. S. Lo, V. S. L'vov, and I. Procaccia, Phys. Rev. E **72**, 016305 (2005).
[16] R. Benzi, E. deAngelis, V. S. L'vov, and I. Procaccia, Phys. Rev. Lett. **95**, 194502 (2005).
[17] R. G. Moser, J. Kim, and N. N. Mansour, Phys. Fluids **11**, 943 (1999); DNS data at http://www.tam.uiuc.edu/Faculty/Moser/channel
[18] C. M. Casciola (private communication).
[19] A. Agrawal, L. Djenidi, and R. A. Antonia, URL http://in3.dem.ist.utl.pt/lxlaser2004/pdf/paper_28_1.pdf.
[20] M. V. Zagarola and A. J. Smits, Phys. Rev. Lett. **78**, 239 (1997).
[21] J. C. Rotta Z. Phys. **129**, 547 (1951).